JOURNAL OF THERMOPHYSICS AND HEAT TRANSFER
Vol. 20, No. 3, July–September 2006

Variable-Gravity Effects on a Single-Phase Partially Confined Spray Cooling System

Kirk L. Yerkes,* Travis E. Michalak,† Kerri M. Baysinger,‡ and Rebekah Puterbaugh§
U.S. Air Force Research Laboratory, Wright–Patterson Air Force Base, Ohio 45433
Scott K. Thomas¶
Wright State University, Dayton, Ohio 45435
and
John McQuillen**
NASA John H. Glenn Research Center at Lewis Field, Cleveland, Ohio 44135

The testing of a single-phase spray cooling system that was flown on the NASA KC-135 Reduced-Gravity Research Aircraft is discussed. An experimental package, consisting of a spray chamber coupled to a fluid delivery loop system, was fabricated for variable gravity flight tests. The spray chamber contains two opposing nozzles spraying on indium tin oxide (ITO) heaters. These heaters are mounted on glass posts that are part of a sump system to remove unconstrained liquid from the test chamber. Thermocouples mounted in and around the posts were used to determine both the heat loss through the underside of the ITO heater and the heat extracted by the spray. During flight tests, for Weber numbers $We = 771 \pm 19$ and 757 ± 15, the nondimensional heat input was varied from $G\Delta = 25$ to 110 for the nondimensional grouping $(Fr^{1/2}Ga)^{1/2} = 20$–66. Flight-test data and terrestrial data were compared to analytical and numerical solutions to evaluate the heat transfer in the heater and support structure. In general, the Nusselt number at the heater surface was found to decrease with increasing $(Fr^{1/2}Ga)^{1/2}$.

Nomenclature

a	=	acceleration level, g
Bi	=	Biot number, $h_{\text{wall}}b/k_{\text{post}}$
b	=	radius of glass heater post assembly, m
D_p	=	droplet diameter, m
Fr	=	Froude number, v^2/aD_p
f	=	heater conduction loss fraction
G	=	$gb^2/[(T_{\text{sat}} - T_{\infty,\text{wall}})k_{\text{htr}}]$
Ga	=	Galileo number, $aD_p^3\rho^2/\mu^2$
$G\Delta$	=	nondimensional heat input, $Q/[\pi bk_{\text{htr}}(T_{\text{sat}} - T_{\infty,\text{wall}})]$
g	=	volumetric heat generation, $Q/\pi b^2\delta$, W/m^3
H	=	glass layer height, m
H_p	=	height of glass post assembly and heater, m
h_{top}	=	spray heat transfer coefficient at top of heater, W/(m^2 · K)
h_{wall}	=	heat transfer coefficient along side of post, W/(m^2 · K)
J_0, J_1	=	Bessel functions
K	=	$k_{\text{fluid}}/k_{\text{htr}}$
k	=	thermal conductivity, W/(m · K)
L	=	height of glass post assembly, m
Nu	=	Nusselt number, $h_{\text{top}}b/k_{\text{fluid}}$
P_{sat}	=	saturation pressure, atm
Q	=	heater input power, W
q	=	heat flux, W/m^2
q_1	=	heat flux lost due to conduction into glass post assembly, $fQ/\pi b^2$, W/m^2
R	=	nondimensional radial coordinate, r/b
r	=	radial coordinate, m
T	=	temperature, °C
T_{int}	=	interface temperature, thermocouple 1 (TC1), located at $z = H_3 + H_4 + H_5$, °C
T_s	=	heater surface temperature, °C
T_{sat}	=	saturation temperature, °C
T_{spray}	=	inlet nozzle temperature, °C
$T_{\infty,\text{top}}$	=	local freestream temperature of liquid flowing over heater surface, °C
$T_{\infty,\text{wall}}$	=	local freestream temperature of liquid flowing along post wall, °C
t	=	time, s
$\dot{V}$	=	volumetric flow rate, m^3/s
$\dot{V}''$	=	volumetric flux, m^3/(m^2 · s)
v	=	droplet velocity, m/s
We	=	Weber number, $\rho v^2 D_p/\sigma$
Z	=	nondimensional axial coordinate, z/b
z	=	axial coordinate, m
γ_n	=	eigenvalue
Δ	=	δ/b
Δ_2	=	H_2/b
δ	=	thickness of indium tin oxide (ITO) heater, m
η_{htr}	=	$bq_1/[(T_{\text{sat}} - T_{\infty,\text{wall}})k_{\text{htr}}]$
η_{post}	=	$bq_1/[(T_{\text{sat}} - T_{\infty,\text{wall}})k_{\text{post}}]$
θ	=	nondimensional temperature, $(T - T_{\infty,\text{wall}})/(T_{\text{sat}} - T_{\infty,\text{wall}})$
θ_{int}	=	$(T_{\text{int}} - T_{\infty,\text{wall}})/(T_{\text{sat}} - T_{\infty,\text{wall}})$
θ_s	=	$(T_s - T_{\infty,\text{wall}})/(T_{\text{sat}} - T_{\infty,\text{wall}})$
$\theta_{\infty,\text{top}}$	=	$(T_{\infty,\text{top}} - T_{\infty,\text{wall}})/(T_{\text{sat}} - T_{\infty,\text{wall}})$
μ	=	absolute viscosity, kg/m · s
ξ	=	L/b

Presented as Paper 2006-0596 at the AIAA 44th Aerospace Sciences Conference, Reno, NV, 9–12 January 2006; received 5 August 2005; accepted for publication 18 November 2005.

*Research Engineer, PRPS, 1950 Fifth Street. Senior Member AIAA.
†Associate Mechanical Engineer, PRPS, 1950 Fifth Street. Member AIAA.
‡Research Assistant, PRPS; also Graduate Research Assistant, Department of Mechanical and Materials Engineering; Wright State University, Dayton, OH 45435; currently MITRE Corporation, Mechanical Engineer, Electronic Systems Center, MS E009, 202 Burlington Road, Bedford, MA 01730. Member AIAA.
§Research Assistant, PRPS; also Graduate Research Assistant, Department of Mechanical and Materials Engineering, Wright State University, Dayton, OH 45435. Member AIAA.
¶Associate Professor, Department of Mechanical and Materials Engineering. Associate Fellow AIAA.
**Aerospace Engineer, Microgravity Fluid Physics Branch.

ρ = density, kg/m^3
σ = surface tension, kg/s^2

Subscripts

fluid = working fluid
htr = region 1, ITO heater
LF = lower film
n = index integers
post = region 2, glass post assembly
UF = upper film
2, 3, 4, 5 = layers 2–5 of glass post assembly

I. Introduction

THE dissipation of thermal energy from current and future electronics for proposed high-power space and air vehicle applications has resulted in the development of thermal management approaches tailored for high heat flux acquisition and high thermal energy transport. Compounding the already difficult thermal problem is the fact that these heat generating sources generally have low thermal masses. This requires special attention be given to the development of robust thermal management approaches that must operate reliably in space and aircraft applications while being subjected to variable body forces resulting from a variable-gravity environment. Recently, the emphasis has been on the development of two-phase cooling concepts to minimize system penalties as compared to the simpler single-phase cooling approaches. Several two-phase thermal management approaches have been or are being considered for space and air vehicle environments. These include two-phase flow and heat transfer,[1,2] pool boiling,[3–5] and spray cooling.[6,7]

Many variable-gravity studies have focused on the physics involved in two-phase flow with heat transfer, and experiments have been performed in drop towers, reduced-gravity aircraft flights, and on orbit. Two-phase, one-component flow with heat transfer in microgravity is seen in many thermal management systems such as flow boiling systems, heat pipes, loop heat pipes, and capillary pumped loops. Work has been done to try to use similarity considerations to scale terrestrial models to predict the behavior of, and to design, prototypes for microgravity.[1,2]

Variable-gravity research on pool boiling with and without subcooling, concentrating on reduced-gravity conditions, has been performed by many researchers.[3–5] It has generally been found that reduced-gravity conditions do not significantly change the heat transfer coefficient for nucleate boiling. However, the critical heat flux (CHF) is generally decreased in a reduced-gravity environment. This reduction in the CHF is, in part, a result of the variation in bubble dynamics due to the lack of buoyancy forces.[5] Observations by Kim et al.[4] showed that small bubbles will coalesce into a large bubble on the surface of the heater in reduced gravity. During subcooled boiling, thermocapillary flows can develop around bubbles, forcing the bubble to the heater surface while drawing warm liquid away from the heater and supplying cool liquid to the heater.[5]

Many researchers have investigated two-phase sprays for the thermal management of devices generating high heat fluxes; however, there has been little research addressing the physics and ultimate performance of two-phase spray cooling in variable-gravity environments. The development of concepts such as spray cooling in these environments must be supported with a sound understanding of the micro- and macroscale two-phase spray thermophysics.

Several variable-gravity spray cooling experiments were performed by Yoshida et al.[6] and Kato et al.[7] onboard a reduced-gravity aircraft. The experiments principally looked at transient and steady-state spray cooling in the low-g portion of the reduced-gravity aircraft flights. A copper block heater was used for transient heat transfer experiments, and a clear thin film indium tin oxide (ITO) heater on a clear base was used for steady-state experiments with flow visualization. The volumetric spray fluxes used were between $\dot{V}'' = 1.36 \times 10^{-4}$ and 3.70×10^{-4} m^3/m$^2 \cdot$ s. These fluxes were low enough that a continuous film of coolant was not allowed to develop on the heater surface. The Weber numbers for their experiments ranged from $We = 28$ to 622, with all but two of the experimental cases having Weber numbers below $We = 60$ (Ref. 6). Fluid management issues that would be encountered for a continuous-flow, closed-loop reduced-gravity spray cooling system were not addressed. No attempt was made during the experiments to retrieve and reuse the working fluid in a closed-loop system.

Baysinger et al.[8] presented the design and preliminary testing of a variable-gravity spray cooling experiment. To build on the work of the previously mentioned researchers, the primary purpose of the study by Baysinger et al. was to investigate heat transfer and fluid management issues for a continuous-flow, closed-loop spray cooling system subjected to a variable-gravity environment. Tests were conducted onboard the NASA KC-135 Reduced-Gravity Research Aircraft, which provided the variable-gravity environment by following a parabolic flight trajectory. Emphasis was placed on developing an initial transient analytical model to predict temperatures and the spray heat transfer coefficient within the heated region of the experiment for low heat loads. The flow rate was sufficient to keep the heater surface completely immersed in the working fluid.

The objective of the present investigation is to continue the work presented by Baysinger et al.,[8] and to investigate the effects of variable-gravity on single-phase spray cooling by varying the nondimensional heat input ($G\Delta = 30$–110) for the nondimensional grouping $(Fr^{1/2}Ga)^{1/2} = 20$–66. Fluid management and heat transfer thermophysics were investigated for Weber numbers $We = 771$ and 757.

II. Experimental Design

The experimental apparatus consists of two primary components similar to that described by Baysinger et al.[8] The first component was a spray test chamber containing two glass heater posts, two spray nozzles, a primary condenser surface, and two sump configurations to collect the liquid and condensate. The second component consisted of a flow loop to manage the working fluid (FC-72) and a water loop used to control the temperature of the spray test chamber. A photograph of the overall experimental apparatus is shown in Fig. 1a. Figure 1b shows the spray test chamber, which was a cylinder having interior dimensions 20.2 cm (7.97 in.) in diameter and 15.2 cm (6 in.) in length. It was made of standard vacuum components to provide a leak-tight environment for the spray cooling experiment.

Each glass heater post assembly was cylindrical with a diameter of 0.016 m, and consisted of five layers, as shown in Fig. 2. The first layer was a thin-film, transparent, ITO heater, which was sputter deposited onto the second layer, a 0.5-mm-thick fused silica substrate. This combination was chosen due to its low thermal mass and to match the coefficient of thermal expansion as closely as possible between the ITO layer and the glass layer to prevent delamination. The low thermal mass of the ITO heater resulted in a rapid response time, such that the system could reach steady-state conditions during the parabolic flight profile, which typically lasted from 20 to 25 s. The heater/substrate was mounted onto a 1-mm-thick wafer of borosilicate glass using optical cement. This subassembly was then adhered to an identical 1-mm-thick wafer of borosilicate glass, which was finally cemented to the main glass post, which was also made of borosilicate glass. The purpose of the two intermediate layers was to allow for channels to position thermocouples, as shown in Fig. 2b. The heater post assembly also allowed for an optical path for visual observation of the heater surface. A preliminary analysis was used to predict temperatures throughout the post to determine the best placement for the thermocouples. The glass heater post assembly was integrated into a sump configuration with a containment cap, located adjacent to each nozzle, and served to remove excess fluid from the chamber and spray surface through an annulus between the heater post and sump wall, as shown in Fig. 3.

The spray nozzle characteristics were evaluated using a two-axis phase Doppler anemometer to determine spray uniformity and droplet size distribution as described by Baysinger et al.[8] Typical droplet velocities, mean droplet diameters, and nozzle pressures are shown in Table 1. The distance from the nozzle to the heater surface was set to approximately 1.0–1.5 cm. This distance was based on a spray cone angle of 60 deg such that the spray contacted only

the heater surface with minimal overspray. The design and placement of the nozzle in relation to the heater cap, heater, and annular sump entrance, shown in Fig. 3b, allowed for vapor generated at the heater surface to be transported past the nozzle into the test chamber interior or entrained with the liquid through the sump annulus. In addition, excess liquid, either due to droplet bounce or flooding, could be transported past the nozzle into the test chamber interior.

Excess vapor and liquid in the chamber were controlled by an annular wick structure, both to aid in condensation and to contain the condensate, as shown in Fig. 1b. The wick structure was formed by lining the internal chamber wall with one layer each of 100 and 150 stainless steel mesh, with the 150 mesh being nearest the wall. An additional cylindrical screen was placed in the chamber interior to provide for an annular space between the screen and the chamber wall. This annular space between the chamber wall and inner screen was filled with stainless-steel wool to help confine the unconstrained liquid in the reduced-gravity environment. In addition, a pressure transducer was installed to measure the vapor pressure within the chamber but external to the annular wick structure. Transient variation in acceleration throughout the flight profile was monitored using a triaxis accelerometer, with an uncertainty of $\pm 0.03\ g$, mounted onto the test chamber. For this investigation, the lower nozzle was operated in a vertical orientation spraying downward onto the heater substrate.

Table 1 Nozzle performance characteristics (droplet diameter and velocity measured ∼15 mm from nozzle)

Volumetric flow rate $\dot{V}$, m^3/s/gph	Nozzle pressure, kPa/psig	Average droplet diameter D_p, μm	Average droplet velocity v, m/s
7.36×10^{-6}/7.0	248/36	48	9.0
1.01×10^{-5}/9.6	324/47	48	12.0
1.21×10^{-5}/11.5	469/68	47	15.0

Figure 4 shows a schematic diagram of the fluid loops. Temperatures throughout the fluid loops were monitored using type E thermocouples that were 0.16 cm (0.0625 in.) in diameter. Key thermocouple locations include the entrances and exits of the test chamber,

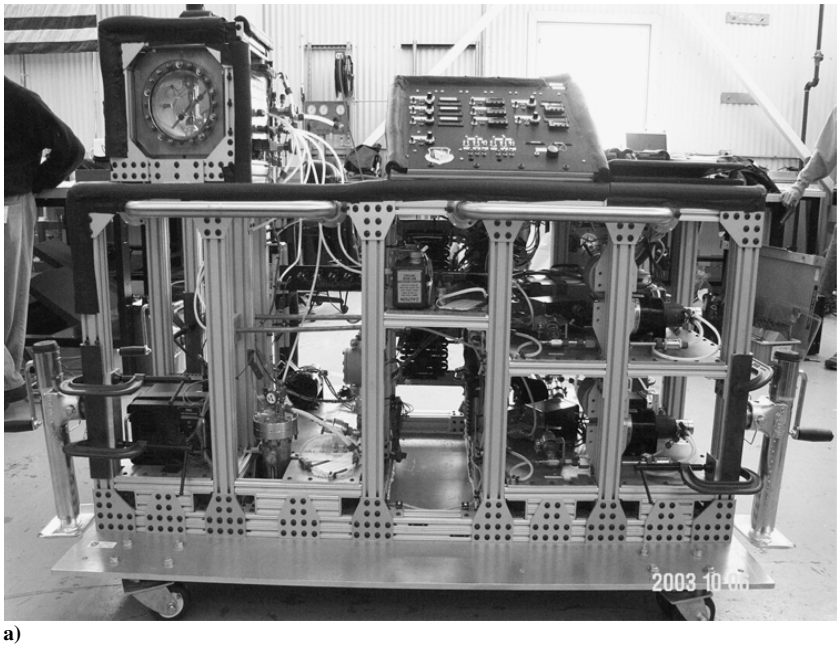

a)

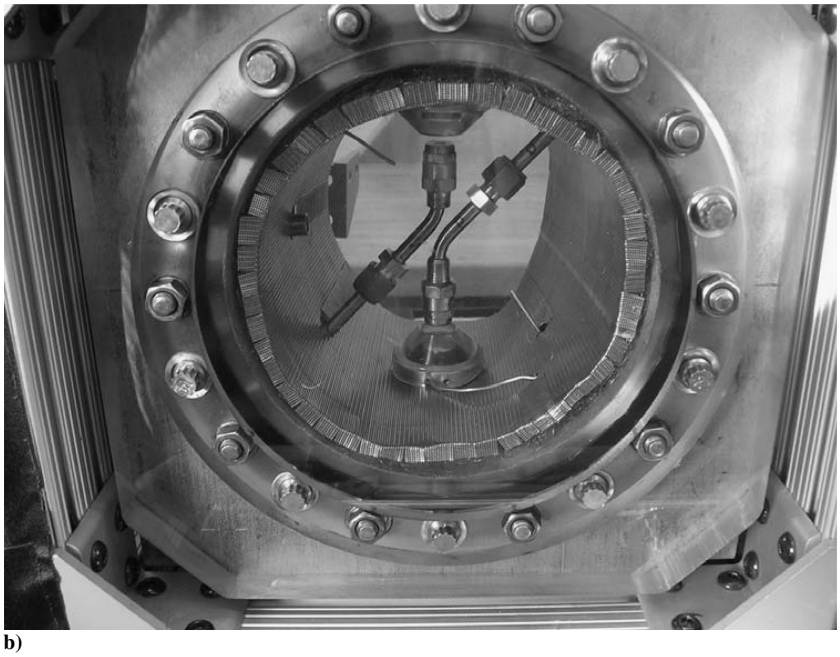

b)

Fig. 1 Experimental flight package showing a) complete package as flown and b) test chamber.

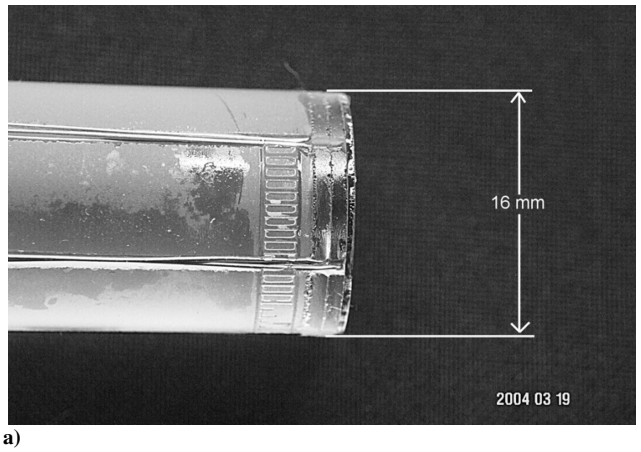

a)

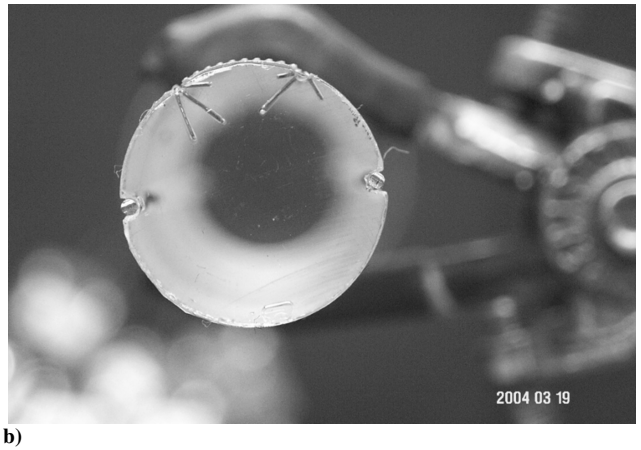

b)

Fig. 2 Magnified view of heater region showing a) side view with glass layers and b) top view with thermocouples.

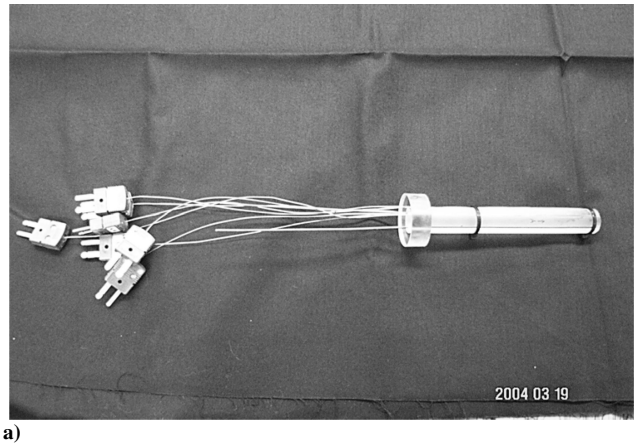

a)

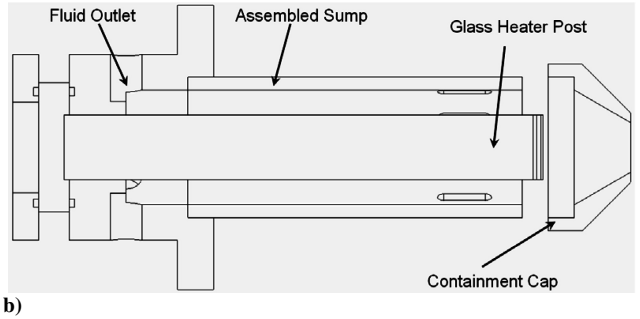

b)

Fig. 3 Assembled glass heater post showing a) thermocouples installed and b) assembled sump with glass heater post and containment cap.

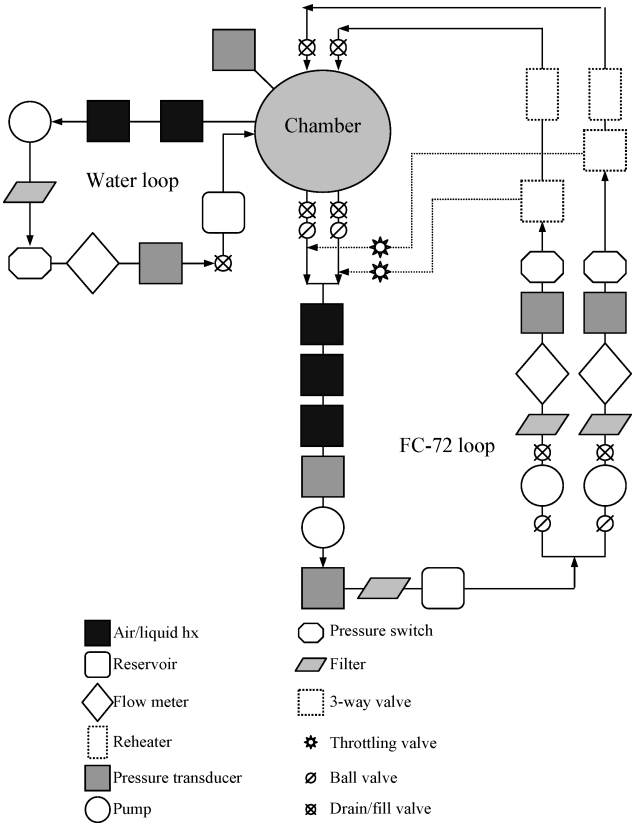

Fig. 4 Flow loop schematic for experimental flight package.

reservoirs, and heat exchanger assemblies. A positive displacement scavenging pump was used to pump the FC-72 working fluid from the sumps through a series of three air/liquid heat exchangers to a reservoir. Pressure transducers were placed on either side of the pump, and the fluid passed through a 40-μm filter before reaching the reservoir. The reservoir served as a volume for the scavenging pump to dump subcooled FC-72 working fluid and a pickup reservoir for the nozzle pumps. Following the reservoir, the fluid branched off into two identical flowpaths, one for each spray nozzle. Each branch consisted of a positive displacement pump followed by a 15-μm filter, a flow meter, a pressure transducer, and a pressure switch. Electrically actuated ball valves were placed at the entrance and exit of each branch to permit isolation of the test chamber. All testing was done with subcooled fluid at ambient temperature.

The experiment was operated and monitored with a control panel and data acquisition system. The data acquisition system consisted of a laptop computer mounted to the top of the experimental package, coupled with a data acquisition/switch unit. Temperature measurements were obtained throughout the chamber, heater post, and within the sump annulus using sheathed thermocouples. Thermocouples (type E, 0.16-cm diameter, time constant $<$4.0 s) were placed in the chamber to measure chamber wall and vapor temperatures. Two thermocouples were placed at the edge of the heater to measure the liquid temperature exiting off of the heater surface T_{UF} and in the sump annulus, approximately 1.27 cm below the heater surface T_{LF}. These temperatures were used to calculate the localized average freestream temperature flowing over the heater surface $T_{\infty,\mathrm{top}}$ and flowing over the pedestal wall ($T_{\infty,\mathrm{wall}}$). Smaller thermocouples (type E, 0.0254-cm diameter, time constant $<$0.5 s), were mounted within the glass heater post assembly. Figure 5 shows the geometrical placement of the thermocouples 1, 2, and 3 (TC1, TC2, and TC3) within the glass heater post. The dimensionless radial and axial locations of the thermocouples are given in Table 2.

For additional stability and accuracy in temperature measurement, the thermocouples within the chamber and glass heater post assembly were referenced to a zero-point reference junction with a stability of $\pm 0.005^{\circ}$C. Thermocouples mounted within the chamber

Table 2 Nondimensional thermocouple locations within glass heater post

Thermocouple number	R	Z_{post}
TC1	0.5875	0.0625
TC2	0.5875	0.1875
TC3	0.875	0.1875

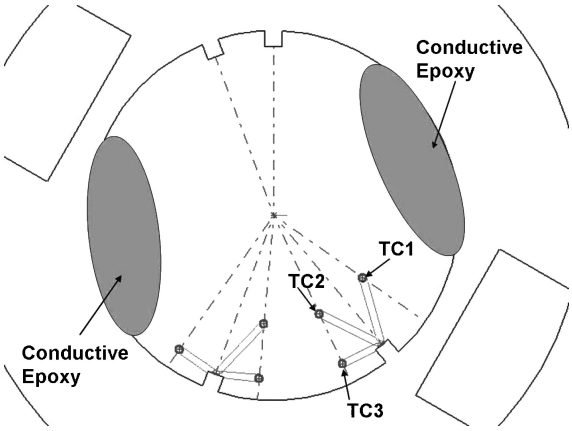

Fig. 5 Thermocouple placement within glass heater post.

and glass heater posts were calibrated using a resistance temperature detector temperature probe and a constant temperature bath in the temperature range from 35 to 120°C. Resulting thermocouple calibrations yielded an uncertainty of ±0.02°C. Heater power was monitored using voltage measurements with an uncertainty of ±0.05% across the heater and a precision resistor with a resistance of 0.10 Ω ± 0.02%, resulting in a heater power measurement error of ±0.07%.

The flow rate of FC-72 through the nozzle was set at a fixed nominal flow rate and monitored throughout the experiment. The flow meters were calibrated, using FC-72, to an average uncertainty of ±3.0% with a maximum uncertainty of ±5.8%. In addition, the percent volume of dissolved air in the FC-72 was measured using a mercury aire-ometer.

III. Mathematical Formulation

With this particular experimental approach, the convective heat transfer coefficients around the heater post assembly and conduction losses needed to be determined. To quantify the top and wall convective heat transfer coefficients and heat lost due to conduction, numerical and analytical approaches to analyzing the heat transfer in the heater post assembly were employed. Figure 6 shows the solution domain and coordinate systems for the numerical and analytical analyses. For the most general case, the heat transfer coefficient and heat flux on the top surface of the ITO heater may vary along the radial and azimuthal directions. This is due to the spray and heater surface interaction and vapor generation as well as the nonuniformity of the internal heat generation within the ITO heater. Also, the side wall heat transfer coefficient could vary along the vertical and azimuthal directions. Both top and side wall heat transfer coefficients will vary with liquid flow rate.

For the present analysis, the following assumptions were made:

1) The system is under steady-state conditions and is axisymmetric.

2) The thermal conductivity of the fused silica glass layer, the borosilicate glass layers, and the ITO heater are identical because the thermal conductivities of both glass types are approximately equal at 100°C ($k_{\text{htr}} = k_{\text{post}} = k_2 = k_3 = k_4 = k_5$).

3) The heat transfer coefficient on the top surface of the ITO heater is constant across the radius where $h_{\text{top}}(r, z = H_p, t) = \text{const}$.

4) The heat transfer coefficient along the outer radius of the glass heater post assembly is constant where $h_{\text{wall}}(r = b, z, t) = \text{const}$.

5) The contact conductances at the interfaces of the glass layers are infinite, which means that both the temperatures and heat fluxes at these interfaces are continuous.

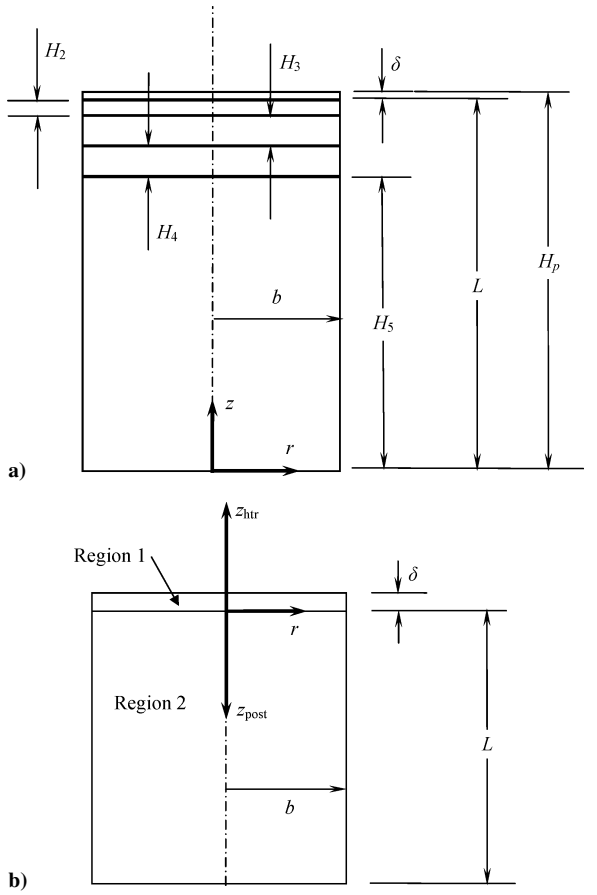

Fig. 6 Glass heater post geometry and coordinate system used for a) numerical model and b) analytical model (not to scale).

6) The temperatures used to define the heat transfer coefficients and evaluate fluid properties are obtained from the experimental data. The freestream temperature to evaluate the spray heat transfer coefficient and fluid properties is defined as the average of the fluid temperature entering the nozzle and the upper film temperature where $T_{\infty,\text{top}} = (T_{\text{spray}} + T_{\text{UF}})/2$.

7) The freestream temperature used to evaluate the heat transfer coefficient on the side of the heater post assembly is the average of the upper and lower film temperatures where $T_{\infty,\text{wall}} = (T_{\text{UF}} + T_{\text{LF}})/2$.

A. Numerical Formulation

A steady-state, axisymmetric numerical model of the cylindrical glass heater post assembly was analyzed using the finite element package ANSYS. The model consisted of several layers, reflecting the structure of the heater, substrate, and post, as well as thermocouple locations within the assembly, as shown in Fig. 6a. Geometric data for the post parameters shown in Fig. 6 are given in Table 3. The thermal conductivity for the entire model was assumed to be $k = 1.04$ W/m · K. To reflect the symmetry of the model, a zero-heat-flux boundary condition was imposed at the centerline of the structure. The spray convection was modeled as a convective heat transfer coefficient h_{top} on the top surface, and the convection from flow down the side walls of the post assembly was represented by a separate convective heat transfer coefficient along the vertical surface, h_{wall}. The bottom of the post was assumed to be adiabatic. The heater was modeled with a volumetric heat generation applied to the top-most layer (ITO) of the model.

For the ITO heater layer, when it is assumed that the thermal properties are constant, the conservation of energy equation is

$$\frac{\partial^2 T_{\text{htr}}}{\partial r^2} + \frac{1}{r}\frac{\partial T_{\text{htr}}}{\partial r} + \frac{\partial^2 T_{\text{htr}}}{\partial z^2} + \frac{g}{k_{\text{htr}}} = 0 \qquad 0 \le r \le b, \qquad L \le z \le H_p \quad (1a)$$

Table 3 Geometric parameters of post

Parameter	Value
δ	1.0 μm
H_2	0.05 ± 0.002 cm
H_3	0.1 ± 0.008 cm
H_4	0.1 ± 0.008 cm
H_5	9.8 ± 0.05 cm
L	10.05 ± 0.07 cm
b	0.79 ± 0.03 cm

where g is the internal heat generation per unit volume due to ohmic heating. The associated boundary conditions are

$$\frac{\partial T_{\text{htr}}}{\partial r} + \frac{h_{\text{wall}}}{k_{\text{htr}}} T_{\text{htr}} = \frac{h_{\text{wall}}}{k_{\text{htr}}} T_{\infty,\text{wall}}, \qquad r = b \tag{1b}$$

$$\frac{\partial T_{\text{htr}}}{\partial z} + \frac{h_{\text{top}}}{k_{\text{htr}}} T_{\text{htr}} = \frac{h_{\text{top}}}{k_{\text{htr}}} T_{\infty,\text{top}}, \qquad z = H_p \tag{1c}$$

$$k_{\text{htr}} \frac{\partial T_{\text{htr}}}{\partial z} = k_2 \frac{\partial T_2}{\partial z}, \qquad T_{\text{htr}} = T_2, \qquad z = L \tag{1d}$$

For the first glass layer, the conservation of energy becomes

$$\frac{\partial^2 T_2}{\partial r^2} + \frac{1}{r}\frac{\partial T_2}{\partial r} + \frac{\partial^2 T_2}{\partial z^2} = 0$$

$$0 \le r \le b, \qquad H_3 + H_4 + H_5 \le z \le L \tag{2a}$$

with boundary conditions

$$\frac{\partial T_2}{\partial r} + \frac{h_{\text{wall}}}{k_2} T_2 = \frac{h_{\text{wall}}}{k_2} T_{\infty,\text{wall}}, \qquad r = b \tag{2b}$$

$$k_{\text{htr}} \frac{\partial T_{\text{htr}}}{\partial z} = k_2 \frac{\partial T_2}{\partial z}, \qquad T_{\text{htr}} = T_2, \qquad z = L \tag{2c}$$

$$k_2 \frac{\partial T_2}{\partial z} = k_3 \frac{\partial T_3}{\partial z}, \qquad T_2 = T_3, \qquad z = H_3 + H_4 + H_5 \tag{2d}$$

For the second glass layer, the conservation of energy becomes

$$\frac{\partial^2 T_3}{\partial r^2} + \frac{1}{r}\frac{\partial T_3}{\partial r} + \frac{\partial^2 T_3}{\partial z^2} = 0$$

$$0 \le r \le b, \qquad H_4 + H_5 \le z \le H_3 + H_4 + H_5 \tag{3a}$$

with boundary conditions

$$\frac{\partial T_3}{\partial r} + \frac{h_{\text{wall}}}{k_3} T_3 = \frac{h_{\text{wall}}}{k_3} T_{\infty,\text{wall}}, \qquad r = b \tag{3b}$$

$$k_2 \frac{\partial T_2}{\partial z} = k_3 \frac{\partial T_3}{\partial z}, \qquad T_2 = T_3, \qquad z = H_3 + H_4 + H_5 \tag{3c}$$

$$k_3 \frac{\partial T_3}{\partial z} = k_4 \frac{\partial T_4}{\partial z}, \qquad T_3 = T_4, \qquad z = H_4 + H_5 \tag{3d}$$

For the third glass layer, the conservation of energy becomes

$$\frac{\partial^2 T_4}{\partial r^2} + \frac{1}{r}\frac{\partial T_4}{\partial r} + \frac{\partial^2 T_4}{\partial z^2} = 0, \qquad 0 \le r \le b, \qquad H_5 \le z \le H_4 + H_5 \tag{4a}$$

with boundary conditions

$$\frac{\partial T_4}{\partial r} + \frac{h_{\text{wall}}}{k_4} T_4 = \frac{h_{\text{wall}}}{k_4} T_{\infty,\text{wall}}, \qquad r = b \tag{4b}$$

$$k_3 \frac{\partial T_3}{\partial z} = k_4 \frac{\partial T_4}{\partial z}, \qquad T_3 = T_4, \qquad z = H_4 + H_5 \tag{4c}$$

$$k_4 \frac{\partial T_4}{\partial z} = k_5 \frac{\partial T_5}{\partial z}, \qquad T_4 = T_5, \qquad z = H_5 \tag{4d}$$

For the fourth glass layer, or glass base, the conservation of energy becomes

$$\frac{\partial^2 T_5}{\partial r^2} + \frac{1}{r}\frac{\partial T_5}{\partial r} + \frac{\partial^2 T_5}{\partial z^2} = 0, \qquad 0 \le r \le b, \qquad 0 \le z \le H_5 \tag{5a}$$

with boundary conditions

$$\frac{\partial T_5}{\partial r} + \frac{h_{\text{wall}}}{k_5} T_5 = \frac{h_{\text{wall}}}{k_5} T_{\infty,\text{wall}} \qquad r = b \tag{5b}$$

$$k_4 \frac{\partial T_4}{\partial z} = k_5 \frac{\partial T_5}{\partial z}, \qquad T_4 = T_5, \qquad z = H_5 \tag{5c}$$

$$\frac{\partial T_5}{\partial z} = 0, \qquad z = 0 \tag{5d}$$

A grid-independence study was performed to ensure adequate meshing of the model. The coarse mesh was determined by the fixed thermocouple locations. For the coarse mesh, the maximum element width in the r direction was $\Delta r = 0.00235$ m. In the z direction, the heater, substrate, and the two thin layers were each one element thick, and the remaining portion of the base was divided into 10 elements, with a spacing ratio of 30, so that the element size increased downward. This produced 56 total elements in the coarse model. The mesh was refined by doubling the number of elements in both directions, with the exception of the heater, where its thickness remained at one element. The result was a fine mesh consisting of 216 elements. For the grid-independence study, typical convective heat transfer coefficient values of $h_{\text{top}} = 10{,}000$ W/(m · K) and $h_{\text{wall}} = 400$ W/(m · K) were chosen, along with a heater power of $Q = 20$ W. Temperatures were recorded at all nodes and compared. The maximum percent difference between the coarse and fine meshes was 0.058%.

B. Analytical Formulation

The analytical formulation was divided into two regions as shown in Fig. 6b. Region 1 is defined as the ITO heater with region 2 being the glass post. Region 1 was formulated as a steady-state one-dimensional heat conduction problem with internal heat generation per unit volume due to resistance heating. The top surface of the heater was treated as a convective boundary condition of the third kind, whereas the lower surface was treated as a heat flux boundary condition of the second kind. Because the lower surface is also the interface between region 1 (ITO heater) and region 2 (glass post), the interface condition must also be satisfied for temperature and heat flux. The dimensional form of the conservation of energy for region 1 is

$$\frac{\mathrm{d}^2 T_{\text{htr}}}{\mathrm{d}z_{\text{htr}}^2} + \frac{g}{k_{\text{htr}}} = 0, \qquad 0 \le z_{\text{htr}} \le \delta \tag{6a}$$

with boundary conditions

$$\frac{\mathrm{d}T_{\text{htr}}}{\mathrm{d}z_{\text{htr}}} + \frac{h_{\text{top}}}{k_{\text{htr}}} T_{\text{htr}} = \frac{h_{\text{top}}}{k_{\text{htr}}} T_{\infty,\text{top}}, \qquad z_{\text{htr}} = \delta \tag{6b}$$

$$\frac{\mathrm{d}T_{\text{htr}}}{\mathrm{d}z_{\text{htr}}} = \frac{q_1}{k_{\text{htr}}}, \qquad T_{\text{htr}} = T_{\text{post}}, \qquad z_{\text{htr}} = 0 \tag{6c}$$

When the nondimensional parameters are defined as

$$\theta = \frac{(T - T_{\infty,\text{wall}})}{(T_{\text{sat}} - T_{\infty,\text{wall}})}, \qquad Z_{\text{htr}} = \frac{z_{\text{htr}}}{b}$$

the nondimensional form of Eqs. (6a–6c) become

$$\frac{\mathrm{d}^2 \theta_{\text{htr}}}{\mathrm{d}Z_{\text{htr}}^2} + G = 0, \qquad 0 \le Z_{\text{htr}} \le \Delta \tag{7a}$$

with boundary conditions

$$\frac{\mathrm{d}\theta_{\text{htr}}}{\mathrm{d}Z_{\text{htr}}} + NuK\theta_{\text{htr}} = NuK\theta_{\infty,\text{top}}, \qquad Z_{\text{htr}} = \Delta \tag{7b}$$

$$\frac{d\theta_{htr}}{dZ_{htr}} = \eta_{htr}, \qquad \theta_{htr} = \theta_{post}, \qquad Z_{htr} = 0 \tag{7c}$$

The nondimensional solution of Eqs. (7a–7c) is given by

$$\theta_{htr}(Z) = -\tfrac{1}{2}GZ^2 + \eta_{htr}Z + [(G\Delta - \eta_{htr})/NuK] + (\Delta/2)(G\Delta - 2\eta_{htr}) + \theta_{\infty,top} \tag{8}$$

Region 2 was formulated as a steady-state two-dimensional conduction problem using both a semi-infinite rod and a finite rod. The top surface is the interface between region 1 (ITO heater) and region 2 (the glass post), satisfying the interface conditions of temperature and heat flux. For the case of the finite rod, the lower surface was treated as an insulated boundary. The side wall of the heater post was treated as a convective boundary condition of the third kind.

1. Semi-Infinite Rod

For the case when region 2 is modeled as a semi-infinite rod, the dimensional form of the conservation of energy is

$$\frac{\partial^2 T_{post}}{\partial r^2} + \frac{1}{r}\frac{\partial T_{post}}{\partial r} + \frac{\partial^2 T_{post}}{\partial z_{post}^2} = 0, \qquad 0 \le r \le b, \quad 0 \le z_{post} \le \infty \tag{9a}$$

with boundary conditions

$$\frac{\partial T_{post}}{\partial r} + \frac{h_{wall}}{k_{post}}T_{post} = \frac{h_{wall}}{k_{post}}T_{\infty,wall}, \qquad r = b \tag{9b}$$

$$\frac{\partial T_{post}}{\partial z_{post}} = \frac{-q_1}{k_{post}}, \qquad T_{post} = T_{htr}, \qquad z_{post} = 0 \tag{9c}$$

Formulating Eqs. (9a–9c) in the nondimensional form of the conservation of energy results in

$$\frac{\partial^2 \theta_{post}}{\partial R^2} + \frac{1}{R}\frac{\partial \theta_{post}}{\partial R} + \frac{\partial^2 \theta_{post}}{\partial Z_{post}^2} = 0, \quad 0 \le R \le 1, \quad 0 \le Z_{post} \le \infty \tag{10a}$$

with boundary conditions

$$\frac{\partial \theta_{post}}{\partial R} + Bi\theta_{post} = 0, \qquad R = 1 \tag{10b}$$

$$\frac{\partial \theta_{post}}{\partial Z_{post}} = -\eta_{post}, \qquad \theta_{post} = \theta_{htr}, \qquad Z_{post} = 0 \tag{10c}$$

where $R = r/b$. The nondimensional solution for the semi-infinite rod becomes

$$\theta_{post}(R, Z) = 2Bi\eta_{post}\sum_{n=1}^{\infty}\frac{e^{-\gamma_n Z}J_0(\gamma_n R)}{J_0(\gamma_n)(Bi^2 + \gamma_n^2)\gamma_n} \tag{11}$$

where the γ_n are positive roots of

$$Bi\,J_0(\gamma_n) = \gamma_n J_1(\gamma_n)$$

2. Finite Rod

When region 2 is modeled as a finite rod of length L, the dimensional form of the conservation of energy is

$$\frac{\partial^2 T_{post}}{\partial r^2} + \frac{1}{r}\frac{\partial T_{post}}{\partial r} + \frac{\partial^2 T_{post}}{\partial z_{post}^2} = 0, \qquad 0 \le r \le b, \quad 0 \le z_{post} \le L \tag{12a}$$

with boundary conditions

$$\frac{\partial T_{post}}{\partial r} + \frac{h_{wall}}{k_{post}}T_{post} = \frac{h_{wall}}{k_{post}}T_{\infty,wall}, \qquad r = b \tag{12b}$$

$$\frac{\partial T_{post}}{\partial z_{post}} = \frac{-q_1}{k_{post}}, \qquad T_{post} = T_{htr}, \qquad z_{post} = 0 \tag{12c}$$

$$\frac{\partial T_{post}}{\partial z_{post}} = 0, \qquad z_{post} = L \tag{12d}$$

The nondimensional form of Eqs. (12a–12c) becomes

$$\frac{\partial^2 \theta_{post}}{\partial R^2} + \frac{1}{R}\frac{\partial \theta_{post}}{\partial R} + \frac{\partial^2 \theta_{post}}{\partial Z_{post}^2} = 0, \qquad 0 \le R \le 1, \quad 0 \le Z_{post} \le \xi \tag{13a}$$

with boundary conditions

$$\frac{\partial \theta_{post}}{\partial R} + Bi\theta_{post} = 0, \qquad R = 1 \tag{13b}$$

$$\frac{\partial \theta_{post}}{\partial Z_{post}} = -\eta_{post}, \qquad \theta_{post} = \theta_{htr}, \qquad Z_{post} = 0 \tag{13c}$$

$$\frac{\partial \theta_{post}}{\partial Z_{post}} = 0, \qquad Z_{post} = \xi \tag{13d}$$

The solution to Eqs. (13a–13c) for region 2 as a finite rod becomes

$$\theta_{post}(R, Z) = 2Bi\eta_{post}\sum_{n=1}^{\infty}\frac{J_0(\gamma_n R)\cosh[\gamma_n(\xi - Z)]}{J_0(\gamma_n)\sinh(\gamma_n \xi)\left(Bi^2 + \gamma_n^2\right)\gamma_n} \tag{14}$$

where the γ_n are the positive roots of

$$Bi\,J_0(\gamma_n) = \gamma_n J_1(\gamma_n)$$

Analytical solution errors can result from interface matching boundary conditions, that is, temperature matching, the number of eigenvalues, and whether the semi-infinite or finite formulation is used. For this problem, the region 1 (ITO heater) and region 2 (glass post) were coupled through the interface conditions of heat flux and temperature. The temperature at the top surface of region 2 was averaged over 100 evenly spaced locations and compared to the temperature at the base of region 1. Temperature matching was performed by varying the fraction of heat flux lost through the base of the heater q_1. The criterion for matching the interface temperature was set to less than 0.01°C. Solutions were calculated using 30 eigenvalues. These solutions were verified to be independent of the number of eigenvalues by increasing the number of eigenvalues to 50. This resulted in a maximum change in temperatures of less than 0.01°C. In addition, solutions using the semi-infinite and finite rod formulations, Eqs. (11) and (14), were also compared and found to have differences of less than 0.01°C.

IV. Results and Discussion

A. Baseline Tests

Terrestrial $(1 - g)$ baseline tests were run to evaluate and quantify the conduction losses through the heater post assembly.[9,10] The bottom nozzle with the upward facing heater was operated using FC-72, which had a measured air content of 20–30% by volume, as the working fluid. When the conduction losses are known, the heat extracted by the spray can be calculated using a simple energy balance. Both the numerical and analytical formulations were used to calculate the temperature distribution within the heater post at three locations coinciding with the thermocouple locations shown in Fig. 5 and Table 2. Numerical and analytical solutions for varying Nusselt and Biot numbers were calculated for a nominal fixed flow rate [$\dot{V} = 5.26 \times 10^{-6}$, 8.41×10^{-6}, and 1.05×10^{-5} m^3/s (5.0, 8.0, and 10.0 gph)] and heat input ($Q = 20$, 30, and 50 W) and then compared with experimental results.

Figures 7 and 8 show examples of the numerical and analytical solutions compared to the nondimensional experimental temperatures $\theta 1$, $\theta 2$, and $\theta 3$, corresponding to TC1, TC2, and TC3, respectively. As would be expected, the temperature is least affected by a variation of Biot number at a location toward the center of the post and closest to the heater, as shown in Figs. 7a and 8a, that corresponds to TC1. At locations farther from the heater, that is, TC2 (Figs. 7b and 8b), the Biot number begins to influence the temperature. The greatest variation in temperature is at the location corresponding to TC3 (Figs. 7c and 8c). The temperatures predicted by the analytical

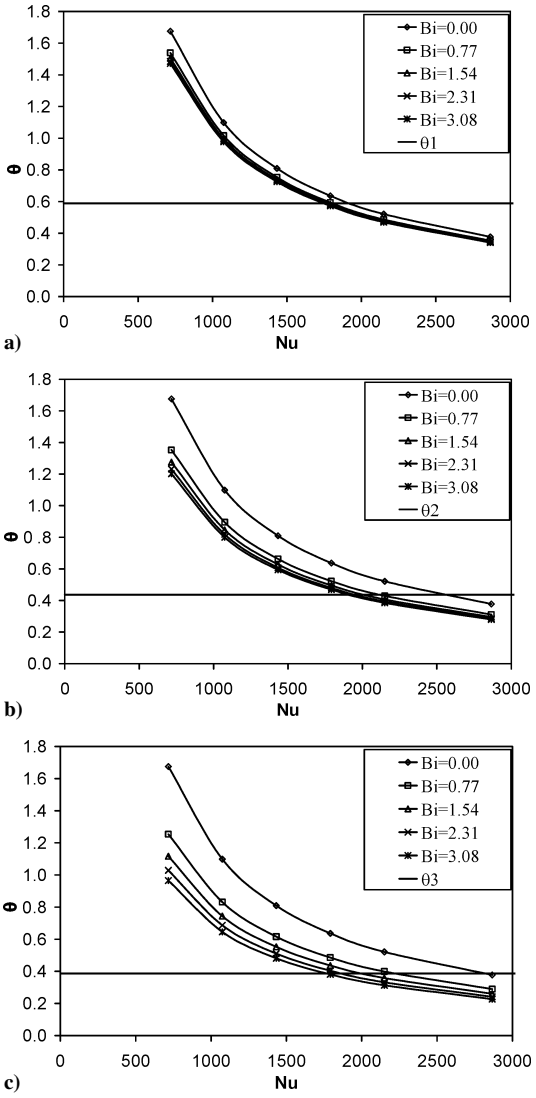

Fig. 7 Numerical results for $Q = 50.5$ W at $\dot{V} = 8.41 \times 10^{-6}$ m^3/s (8.0 gph) for temperature locations corresponding to a) TC1, b) TC2, and c) TC3.

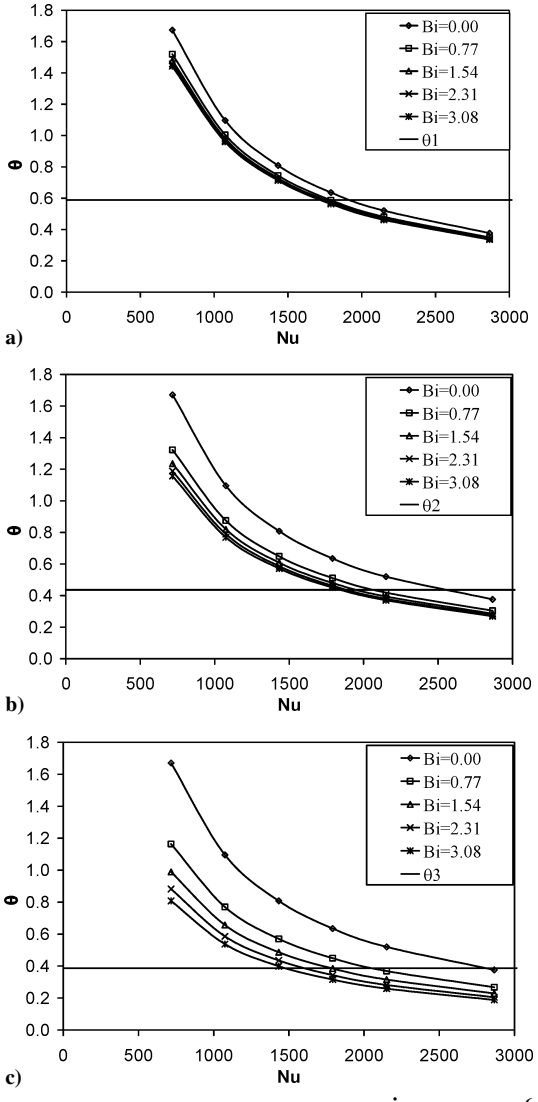

Fig. 8 Analytical results for $Q = 50.5$ W at $\dot{V} = 8.41 \times 10^{-6}$ m^3/s (8.0 gph), for temperature locations corresponding to a) TC1, b) TC2, and c) TC3.

solutions were consistently lower than those of the numerical solutions. This is most evident by comparing Figs. 7c and 8c, where this difference is the greatest, with increasing Biot number. This is most probably due to how the interface condition was treated in the analytical formulation.

Both the numerical and analytical solutions were then used to find the fraction of heat lost due to conduction through the heater post assembly. For the numerical solution, the energy balance at the top surface of the heater

$$G\Delta = NuK(\theta_s - \theta_{\infty,\text{top}}) \tag{15}$$

was used to determine the heat extracted by the spray. The estimated Nusselt number was determined from Fig. 7 at the intersection of the experimental temperatures $\theta 1$, $\theta 2$, and $\theta 3$ and the numerical results for varying Nusselt and Biot numbers. The local freestream temperature $\theta_{\infty,\text{top}}$ was the experimentally measured film temperature across the top of the heater. The surface temperature $\theta_s(r)$ was determined from the numerical solutions and was either treated as a single-point temperature corresponding to a location directly above TC1 or as an average across the heater surface. The fraction of heat lost f was determined as the ratio of heat conducted down the pedestal to the input heat of the ITO heater.

In a similar manner, the analytical solutions were used to determine the heat lost through the heater post assembly. The estimated Nusselt number was determined from Fig. 8 at the intersection of the

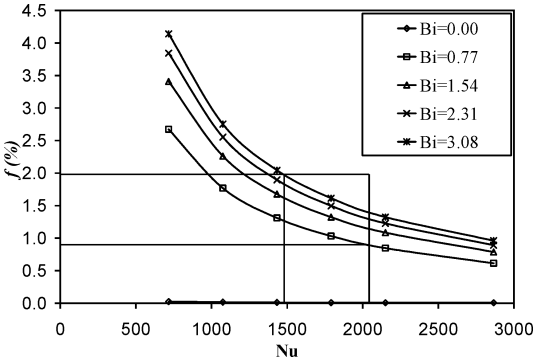

Fig. 9 Graphical determination of conduction losses for range of Nusselt numbers for $Q = 50.5$ W at $\dot{V} = 8.41 \times 10^{-6}$ m^3/s (8.0 gph).

experimental temperatures $\theta 1$, $\theta 2$, and $\theta 3$ and the analytical results for varying Nusselt and Biot numbers. Because the fraction of heat lost was an input variable in the analytical formulation, the conduction losses could be determined. Once a range of Nusselt numbers was determined, the fraction of heat lost could be estimated as shown in Fig. 9.

Figure 10 shows the conduction losses for the three approaches. All three approaches showed good agreement ranging from $f = 1.0$

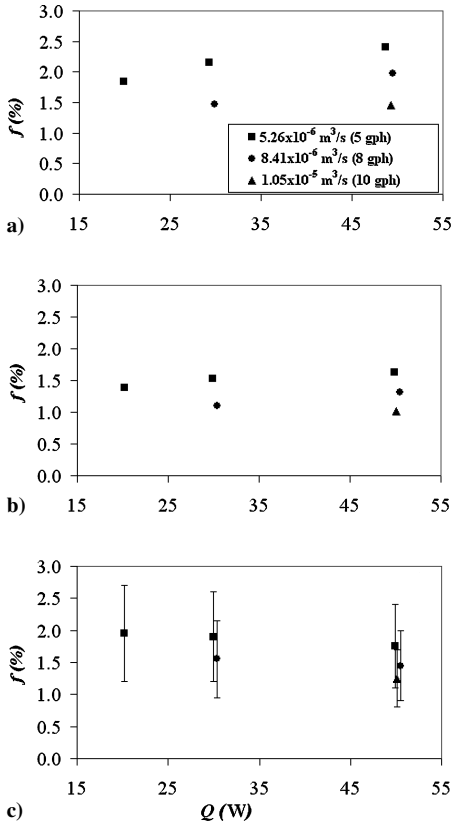

Fig. 10 Heat lost due to conduction through glass heater post assembly based on a) numerical solution based on average surface temperature, b) numerical solution based on surface temperature directly above TC1, and c) analytical solution (direct determination of f).

to 2.5%. This result is consistent with estimates of 1.0% by Baysinger et al.[8] Based on these results, in the subsequent analyses, the fraction of heat loss due to conduction used was $f = 1.5\%$.

B. Flight Tests

Flight tests were conducted aboard NASA's KC-135 Reduced-Gravity Research Aircraft using FC-72, which had a measured air content of 20–30% by volume, as the working fluid. The bottom nozzle with the upward facing heater was operated at nominally fixed Weber numbers of $We = 771 \pm 19$ and 757 ± 15 with an inlet temperature of $T_{\text{spray}} = 23.4 \pm 0.4^{\circ}\text{C}$. Throughout the flight profile, the heater power was varied while the test chamber was maintained at a saturation temperature of $T_{\text{sat}} = 56 \pm 2^{\circ}\text{C}$, which corresponds to a chamber pressure of $P_{\text{sat}} = 1.00 \pm 0.07$ atm. When the Buckingham pi theorem was used, the nondimensional grouping $(Fr^{1/2}Ga)^{1/2}$ was found to be a measure of the ratio of inertia and acceleration forces to the viscous forces. Accelerations generated by a parabolic aircraft flight profile resulted in the variation of this nondimensional grouping $(Fr^{1/2}Ga)^{1/2} = 20$–66.

Experimental data were used to calculate the surface heat flux and Nusselt number using the conduction loss through the heater post of $f = 1.5\%$ as determined from the baseline tests. The Nusselt number was calculated using the one-dimensional energy balance

$$Nu = [1 - f)G\Delta]/\{K[\eta_{\text{post}}\Delta_2 + (\theta_{\text{int}} - \theta_{\infty,\text{top}})]\} \qquad (16)$$

that accounted for the heat loss due to conduction within the post.

For the experiments conducted, Table 4 shows the nondimensional heat input from the heater surface to the spray, $(1 - f)G\Delta$, and the dimensional heat and heat flux from the heater surface to the spray. Figure 11 shows this nondimensional heat input from the heater surface vs the nondimensional temperature drop from the heater surface to the freestream film. The nondimensional temperature drop increases linearly with the nondimensional heat input through $(1 - f)G\Delta \approx 70$. In this portion, there was little effect due

Table 4 Nondimensional heater input to spray and dimensional heater and heat flux input to spray

$(1 - f)G\Delta$	Heat to spray, W	Surface heat flux, W/cm^2
25.07 ± 1.00	20.22 ± 0.16	10.05 ± 0.08
38.38 ± 1.29	29.98 ± 0.39	14.91 ± 0.19
66.18 ± 2.15	49.45 ± 0.23	24.59 ± 0.12
109.92 ± 0.99	79.24 ± 0.23	39.41 ± 0.12

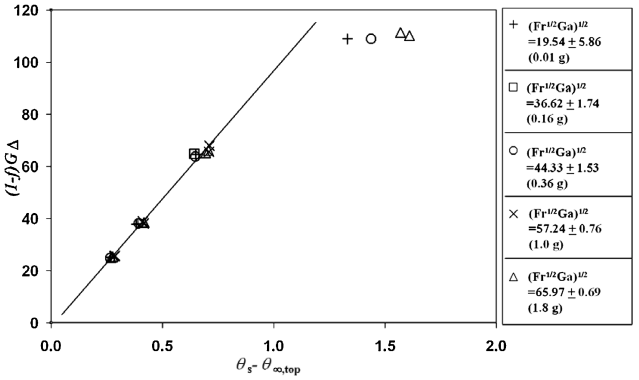

Fig. 11 Nondimensional temperature drop vs $(1 - f)G\Delta$ from heater surface to freestream fluid for varying $(Fr^{1/2}Ga)^{1/2}$.

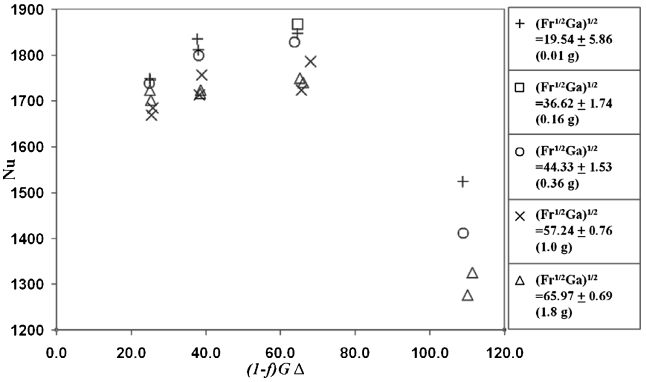

Fig. 12 Nusselt number vs $(1 - f)G\Delta$ for varying $(Fr^{1/2}Ga)^{1/2}$.

to varying $(Fr^{1/2}Ga)^{1/2}$. Increasing the heater input from the heater surface to $(1 - f)G\Delta \approx 110$ resulted in a significant increase in the nondimensional temperature difference between the heater surface temperature and freestream film temperature over and above that predicted by a linear extrapolation. This is most probably due to the initiation of vapor generation at the heater surface and that the freestream film temperature is used as a reference instead of the saturation temperature. The interface temperature at TC1 for this case was close to the saturation temperature of $T_{\text{sat}} = 56 \pm 2^{\circ}\text{C}$. The effect of $(Fr^{1/2}Ga)^{1/2}$ is shown by an increase in the nondimensional temperature drop between the heater surface temperature and freestream film temperature with an increase in $(Fr^{1/2}Ga)^{1/2}$ for the cases $(Fr^{1/2}Ga)^{1/2} = 19.54$, 44.33, and 65.97.

The effect of $(Fr^{1/2}Ga)^{1/2}$ on the Nusselt number is most noticeable as shown in Fig. 12. The Nusselt numbers corresponding to $(Fr^{1/2}Ga)^{1/2} = 19.54$ and 44.33 were consistently higher than the Nusselt numbers corresponding to $(Fr^{1/2}Ga)^{1/2} = 65.97$ for $(1 - f)G\Delta = 25$–110. For the nondimensional heat input from the heater surface of $(1 - f)G\Delta = 110$, the Nusselt number, for all of the values for $(Fr^{1/2}Ga)^{1/2}$, decreased most, probably due to the initiation of vapor generation. However, the Nusselt numbers for $(Fr^{1/2}Ga)^{1/2} = 19.54$ and 44.33 continued to remain higher than the Nusselt number for the $(Fr^{1/2}Ga)^{1/2} = 65.97$ case.

Figure 13 shows Nusselt number vs the nondimensional quantity $(Fr^{1/2}Ga)^{1/2}$ for Weber numbers $We = 771 \pm 19$, for $(1 - f)G\Delta < 80$, and 757 ± 15, for $(1 - f)G\Delta = 110 \pm 1$. For the

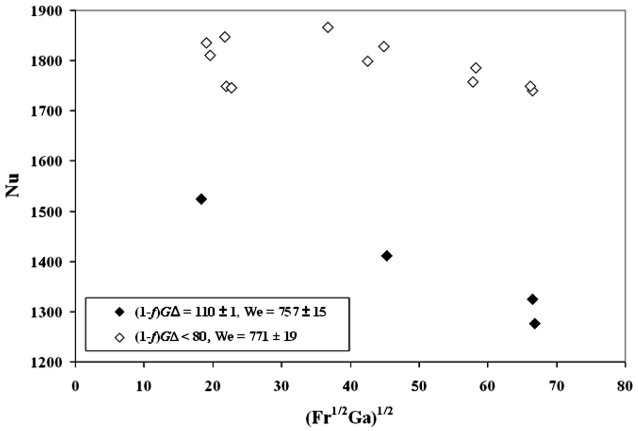

Fig. 13 Nusselt number vs $(Fr^{1/2}Ga)^{1/2}$ for $(1-f)G\Delta < 80$ and $(1-f)G\Delta = 107 \pm 2$.

experimental data shown in Fig. 13, the Nusselt number tended to decrease with increasing $(Fr^{1/2}Ga)^{1/2}$.

V. Conclusions

The effects of variable gravity on single-phase spray cooling with a partially confined geometry have been investigated. In general, the Nusselt number tended to decrease with increasing $(Fr^{1/2}Ga)^{1/2}$ for a nominally fixed Weber number. At this time, the physics driving the observed phenomena are not clearly understood. Some possible reasons may be variation in flow rate, recirculation of the spray film back onto the heater surface, influence of the confined geometry, effects of absorbed air in the FC-72 working fluid, or some unidentified thermophysical phenomena occurring at the heater surface. Regardless of the mechanism, the observed phenomena appear to be amplified at the onset of vapor generation.

Based on these very preliminary results, there appears to be the potential for performance improvement for the application of spray cooling depending on the magnitude of $(Fr^{1/2}Ga)^{1/2}$. However, this investigation only addressed the performance of a single nozzle at a relatively fixed Weber number. It is not known if the implementation of a spray nozzle array will provide a similar performance enhancement. Investigations with single-phase spray cooling for a varying Weber number and the effect of variable gravity on two-phase spray cooling still need to be addressed.

Acknowledgments

This research was conducted as a collaborative effort with the NASA John H. Glenn Research Center at Lewis Field using the blanket interagency agreement SAA3-307 between NASA John H. Glenn Research Center at Lewis Field and the U.S. Air Force Research Laboratory, Order 12.

References

[1]Mudawar, I., "Assessment of High-Heat-Flux Thermal Management Schemes," *IEEE Transactions on Components and Packaging Technologies*, Vol. 24, No. 2, 2001, pp. 122–141.

[2]Delil, A. A. M., "Microgravity Two-Phase Flow and Heat Transfer," *Physics of Fluids in Microgravity*, edited by R. Monti, Taylor and Francis, London, 2001, pp. 263–292.

[3]Kim, J., "Review of Reduced Gravity Boiling Heat Transfer: US Research," *Journal of the Japan Society of Microgravity Application*, Vol. 20, No. 4, 2003, pp. 264–271.

[4]Kim, J., Benton, J. F., and Wisniewski, D., "Pool Boiling Heat Transfer on Small Heaters: Effect of Gravity and Subcooling," *International Journal of Heat and Mass Transfer*, Vol. 45, No. 19, 2002, pp. 3919–3932.

[5]Straub, J., "Pool Boiling and Bubble Dynamics in Microgravity," *Physics of Fluids in Microgravity*, edited by R. Monti, Taylor and Francis, London, 2001, pp. 322–370.

[6]Yoshida, K., Abe, Y., Oka, T., Mori, Y. H., and Nagashima, A., "Spray Cooling Under Reduced Gravity Condition," *Journal of Heat Transfer*, Vol. 123, No. 2, 2001, pp. 309–318.

[7]Kato, M., Abe, Y., Mori, Y. H., and Nagashima, A., "Spray Cooling Characteristics Under Reduced Gravity," *Journal of Thermophysics Heat Transfer*, Vol. 9, No. 2, 1994, pp. 378–381.

[8]Baysinger, K. M., Yerkes, K. L., Michalak, T. E., Harris, R. J., and McQuillen, J., "Design of a Microgravity Spray Cooling Experiment," AIAA Paper 2004-0966, Jan. 2004.

[9]Baysinger, K. M., Yerkes, K. L., and Thomas, S. K., "Experimental Testing and Numerical Modeling of Spray Cooling Under Terrestrial Gravity Conditions," U.S. Air Force Research Lab. Rept. AFRL-PR-WP-TR-2005-2047, Wright–Patterson AFB, OH, 2005.

[10]Baysinger, K. M., "Experimental Testing and Numerical Modeling of Spray Cooling Under Terrestrial Gravity Conditions," M.S. Thesis, Dept. of Mechanical and Materials Engineering, Wright State Univ., Dayton, OH, Nov. 2005.